Collective structures in ^{62}Cu

D. W. Luo,[1,*] C. Xu,[1,*] Y. K. Wang,[1] Z. H. Li,[1,†] R. A. Bark,[2] S. Q. Zhang,[1] H. Hua,[1,‡] S. Y. Wang,[3] J. Peng,[4] X. Q. Li,[1] H. Y. Wu,[1] X. Wang,[1] C. G. Wu,[1] Q. T. Li,[1] J. Lin,[1] Y. Jin,[1] W. Z. Xu,[3] L. Mu,[3] J. Meng,[1] F. R. Xu,[1] Y. L. Ye,[1] D. X. Jiang,[1] P. Jones,[2] E. A. Lawrie,[2,5] P. Papka,[6] M. F. Nkalanga,[2,7] T. D. Bucher,[2] M. V. Chisapi,[2,6] L. Msebi,[2,5] S. Jongile,[2,6] S. Ntshangase,[7] B. R. Zikhali,[5] S. H. Mthembu,[5] T. Seakamela,[8] M. A. Sithole,[2,5] O. Shirihda,[2,9] A. A. Aava,[10] L. Mdletshe,[7] K. L. Malatji,[2,6] S. Mhlongo,[7] and L. Makhathini[2]

[1]*School of Physics and State Key Laboratory of Nuclear Physics and Technology, Peking University, Beijing, 100871, China*
[2]*iThemba LABS, National Research Foundation, P.O. Box 722, Somerset West 7129, South Africa*
[3]*Shandong Provincial Key Laboratory of Optical Astronomy and Solar-Terrestrial Environment, Institute of Space Sciences, Shandong University, Weihai 264209, China*
[4]*Department of Physics, Beijing Normal University, Beijing 100875, China*
[5]*Department of Physics, University of the Western Cape, Private Bag X17, Bellville 7535, South Africa*
[6]*Department of Physics, University of Stellenbosch, Matieland 7602, South Africa*
[7]*Department of Physics, University of Zululand, Private Bag X1001, KwaDlangezwa 3886, South Africa*
[8]*Department of Physics, University of Johannesburg, 2006 Auckland Park, South Africa*
[9]*Department of Physical and Earth Sciences, Sol Plaatje University, Private Bag X5008, Kimberley 8301, South Africa*
[10]*University of the Witwatersrand, 1 Jan Smuts Avenue, Braamfontein 2000, Johannesburg, South Africa*

(Received 16 June 2021; revised 17 October 2021; accepted 11 January 2022; published 7 February 2022)

The spectroscopy of ^{62}Cu is studied via the ^{54}Cr(^{12}C, $1p3n$) ^{62}Cu fusion-evaporation reaction. On the basis of the γ-γ coincidence analysis, angular distributions from oriented states, and linear polarization measurement, three positive-parity and three negative-parity level sequences in ^{62}Cu are observed, including two new γ-ray transitions and one new level. The collective structures are discussed in terms of the tilted axis cranking covariant density functional theory. Although not firmly confirmed in experiment, the properties of a magnetic rotational structure with the $\pi(f_{7/2})^{-1}(p_{3/2}f_{5/2})^2 \otimes \nu(g_{9/2})^1(p_{3/2}f_{5/2})^4$ configuration have been discussed. Its angular momentum generation is probably due to the shears mechanism.

DOI: 10.1103/PhysRevC.105.024305

I. INTRODUCTION

A common feature for the nuclei in the mass $A \approx 60$ region is that moderately deformed or single-particle structures dominate at low spins. They involve the negative-parity $f_{7/2}$, $p_{3/2}$, $f_{5/2}$, and $p_{1/2}$ orbitals. Well-deformed or superdeformed rotational structures occur at relatively high spins where the positive-parity deformation-driving $1g_{9/2}$ orbital plays a crucial role. With particles and holes in high-j shells, such as a neutron in the $\nu g_{9/2}$ shell and a proton hole in the $\pi f_{7/2}$ shell, magnetic rotational structures have also been reported in this region, such as in ^{58}Fe [1] and ^{60}Ni [2], etc. Due to the competition and interplay between the collective and the single-particle degrees of freedom, the level schemes in these nuclei are very complex but provide a good opportunity to test the predictions of different theoretical models.

For the Cu isotopes lying above the doubly magic nucleus ^{56}Ni, well-deformed and superdeformed structures have been observed in ^{58}Cu [3],^{59}Cu [4], and ^{61}Cu [5] isotopes. So far, although the structure of the heavier ^{62}Cu nucleus has been studied in a variety of experiments [6], including heavy-ion fusion-evaporation studies [7,8], no obvious collective structures have been reported. The observed energy spectra were interpreted in terms of the interacting boson-fermion-fermion model [7] and the shell model [8]. Here, we report an experimental investigation of the level structures in ^{62}Cu via the ^{54}Cr(^{12}C, $1p3n$) ^{62}Cu fusion-evaporation reaction. Three negative-parity and three positive-parity level sequences in ^{62}Cu are observed, including two new γ-ray transitions and one new level. The collective structures of these sequences are discussed in terms of systematic comparison and the tilted axis cranking covariant density functional theory (TAC-CDFT) [9].

II. EXPERIMENT

The present experiment was performed at the Separated Sector Cyclotron of iThemba LABS in South Africa. High-spin states of ^{62}Cu were populated via the ^{54}Cr(^{12}C, $1p3n$) ^{62}Cu fusion-evaporation reaction at a beam energy of 67 MeV. The target consisted of a 0.72 mg/cm^2 ^{54}Cr foil with a 18.80 mg/cm^2 Au backing. In-beam γ rays were measured with the AFRODITE array [10],

*These authors equally contributed to this paper.
†zhli@pku.edu.cn
‡hhua@pku.edu.cn

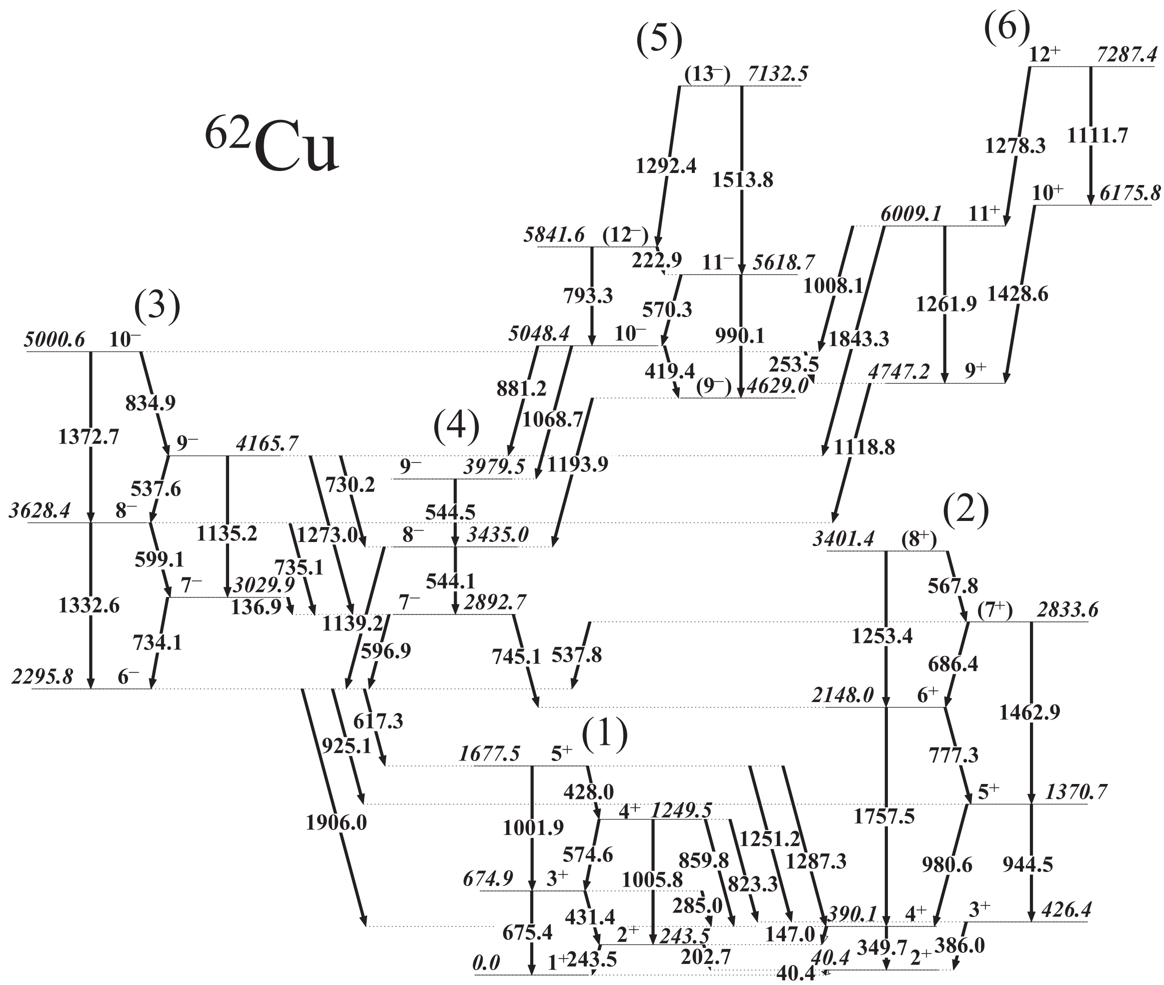

FIG. 1. Partial level scheme of ^{62}Cu. Energies are in keV.

which consisted of 11 Compton-suppressed clover detectors and three low-energy photon spectrometers at the time of the experiment. The efficiency of the each clover is 0.2% at the ^{60}Co energy of 1.33 MeV. The clover detectors were arranged in two rings at 90° (seven clovers) and 135° (four clovers) with respect to the beam direction.

Approximately 8.34×10^9 γ-γ coincident events were collected from which a symmetric matrix was built. The level scheme analysis was performed using the RADWARE package [11]. To determine the multipolarities of the γ-ray transitions, two asymmetric angular distributions from oriented states (ADO) [12] matrices were constructed by using the γ rays detected at all angles (the y axis) against those detected at 90° and 135° (the x axis), respectively. The multipolarities of the emitted γ rays were analyzed by means of the ADO ratio, which was defined as I_γ (135°)/I_γ (90°). The typical ADO ratios for stretched quadrupole and stretched pure dipole transitions are found to be $\approx$1.2 and $\approx$0.8, respectively. Furthermore, to distinguish the electric and magnetic characters of the γ rays, linear polarization measurements [13] were performed using the seven clover detectors positioned at 90° relative to the beam direction as Compton polarimeters. The linear polarization P is defined as

$$P = \frac{A}{Q}, \tag{1}$$

where

$$A = \frac{N_\perp - N_\parallel}{N_\perp + N_\parallel}, \tag{2}$$

and Q is the polarization sensitivity for the clover detectors, which is a function of the γ-ray energy [13]. $N_\perp$ and $N_\parallel$ denote the number of events scattered perpendicular and parallel to the beam direction, respectively.

III. RESULTS AND DISCUSSION

The partial level scheme of ^{62}Cu deduced from the present work is shown in Fig. 1. It was constructed from the γ-γ coincidence relationships, intensity balances, ADO ratios, and linear polarizations. The results are summarized in Table I. Most of the levels in ^{62}Cu have been observed in many previous experiments [6]. The present analyses confirm these levels and support the previous spin-parity assignments. Two new

TABLE I. γ-ray energies, excitation energies, relative γ-ray intensities, ADO ratios, the linear polarizations, and spin-parity assignments in ^{62}Cu.

E_γ (keV)	E_i (keV)	E_f (keV)	Relative intensity	R_{ADO}	Linear polarization	$I_i^\pi \rightarrow I_f^\pi$
40.4(5)	40.4	0				$2^+ \rightarrow 1^+$
136.9(2)	3029.9	2892.7	0.55(9)	1.30(29)		$7^- \rightarrow 7^-$
147.0(3)	390.1	243.5	3.69(45)	1.25(4)		$4^+ \rightarrow 2^+$
191.8(3)[a]	1677.5	1485.7				$5^+ \rightarrow 4^+$
202.7(2)	243.5	40.4	4.47(54)			$2^+ \rightarrow 2^+$
222.9(2)[a]	2518.5	2295.8	0.74(22)			$6^- \rightarrow 6^-$
222.9(1)	5841.6	5618.7	0.63(16)	0.81(8)		$(12^-) \rightarrow 11^-$
243.5(1)	243.5	0	7.69(184)			$2^+ \rightarrow 1^+$
243.7(1)[a]	3435.0	3191.4	4.40(82)			$8^- \rightarrow 6^-$
243.8(1)[a]	1921.6	1677.5				$(5^+) \rightarrow 5^+$
253.5(1)	5000.6	4747.2	0.72(11)	0.60(6)		$10^- \rightarrow 9^+$
272.9(8)[a]	699.3	426.4	0.18(6)	0.76(5)		$3^+ \rightarrow 3^+$
285.0(1)	674.9	390.1	0.50(8)	0.76(8)		$3^+ \rightarrow 4^+$
335.6(5)[a]	7620.5	7287.4	0.42(7)			$(12^+) \rightarrow 12^+$
349.7(2)	390.1	40.4	100.00	1.23(9)	0.59(8)	$4^+ \rightarrow 2^+$
358.2(6)[a]	8960.8	8602.6				$(14^+) \rightarrow (13^+)$
378.4(2)[a]	2295.8	1917.5	0.25(4)	0.46(1)		$6^- \rightarrow 5^+$
386.0(5)	426.4	40.4	12.13(147)	0.66(2)	−0.73(9)	$3^+ \rightarrow 2^+$
403.9(1)[a]	5000.6	4597.6	1.51(24)			$10^- \rightarrow 10^-$
419.4(2)	5048.4	4629.0	7.69(120)	0.92(2)		$10^- \rightarrow (9^-)$
428.0(2)	1677.5	1249.5	2.45(38)	0.72(2)		$5^+ \rightarrow 4^+$
431.4(2)	674.9	243.5	1.53(24)	0.72(2)		$3^+ \rightarrow 2^+$
438.6(1)[a]	3628.4	3191.4	4.15(65)			$8^- \rightarrow 6^-$
467.6(2)[a]	4447.6	3979.5	2.52(39)	0.60(2)		$9^- \rightarrow 9^-$
476.7(2)[a]	4105.1	3628.4	3.32(52)	0.71(2)		$9^- \rightarrow 8^-$
487.8(1)[a]	4165.7	3675.2	0.81(13)			$9^- \rightarrow 8^-$
492.5(3)[a]	4597.6	4105.1	3.83(60)	0.56(2)	−0.27(15)	$10^- \rightarrow 9^-$
519.3(1)[a]	7620.5	7101.6	1.79(28)	0.52(2)	0.37(24)	$(12^+) \rightarrow 12^+$
537.6(1)	4165.7	3628.4	1.71(32)			$9^- \rightarrow 8^-$
537.8(2)	2833.6	2295.8	4.89(119)			$(7^+) \rightarrow 6^-$
544.1(2)	3435.0	2892.7	3.04(74)			$8^- \rightarrow 7^-$
544.5(2)	3979.5	3435.0	19.94(374)	0.78(1)		$9^- \rightarrow 8^-$
567.8(5)	3401.4	2833.6	0.73(14)			$(8^+) \rightarrow (7^+)$
570.3(2)	5618.7	5048.4	5.98(94)	0.60(2)	−0.43(21)	$11^- \rightarrow 10^-$
574.6(8)	1249.5	674.9	2.12(45)			$4^+ \rightarrow 3^+$
596.9(2)	2892.7	2295.8	56.70(887)	0.72(3)	0.15(4)	$7^- \rightarrow 6^-$
599.1(8)	3628.4	3029.9	1.23(23)			$8^- \rightarrow 7^-$
601.1(8)[a]	5048.4	4447.6				$10^- \rightarrow 9^-$
617.3(3)	2295.8	1677.5	3.15(49)	0.58(2)	1.95(32)	$6^- \rightarrow 5^+$
660.7(2)[a]	5108.3	4447.6	5.35(84)	0.69(9)		$(10^-) \rightarrow 9^-$
675.4(8)	674.9	0				$3^+ \rightarrow 1^+$
686.4(2)	2833.6	2148.0	2.24(42)			$(7^+) \rightarrow 6^+$
689.0(2)[a]	6530.6	5841.6	4.12(65)			$(13^-) \rightarrow (12^-)$
713.1(3)[a]	7243.7	6530.6	3.05(48)			$(14^-) \rightarrow (13^-)$
730.2(3)	4165.7	3435.0	2.50(39)			$9^- \rightarrow 8^-$
734.1(5)	3029.9	2295.8	8.26(174)			$7^- \rightarrow 6^-$
735.1(1)	3628.4	2892.7	4.84(89)			$8^- \rightarrow 7^-$
745.1(2)	2892.7	2148.0	1.01(16)			$7^- \rightarrow 6^+$
777.3(2)	2148.0	1370.7	6.63(104)	0.77(2)	0.38(20)	$6^+ \rightarrow 5^+$
782.5(4)[a]	3675.2	2892.7	5.61(88)	0.45(2)	−0.37(32)	$8^- \rightarrow 7^-$
789.2(2)[a]	3979.5	3191.4	1.65(26)			$9^- \rightarrow 6^-$
793.3(1)	5841.6	5048.4	1.79(28)		0.33(37)	$(12^-) \rightarrow 10^-$
811.2(2)[a]	5258.8	4447.6	2.30(36)	0.56(2)		$(10^-) \rightarrow 9^-$
823.3(1)	1249.5	426.4	1.33(21)	0.73(1)	−0.39(15)	$4^+ \rightarrow 3^+$
834.9(2)	5000.6	4165.7	7.73(121)		0.39(13)	$10^- \rightarrow 9^-$
859.8(3)	1249.5	390.1	2.51(39)			$4^+ \rightarrow 4^+$

TABLE I. *(Continued.)*

E_γ (keV)	E_i (keV)	E_f (keV)	Relative intensity	R_{ADO}	Linear polarization	$I_i^\pi \rightarrow I_f^\pi$
881.2(3)	5048.4	4165.7	4.39(69)			$10^- \rightarrow 9^-$
895.5(3)[a]	5000.6	4105.1	3.28(51)			$10^- \rightarrow 9^-$
925.1(2)	2295.8	1370.7	91.45(1109)	0.82(2)	0.64(8)	$6^- \rightarrow 5^+$
944.5(2)	1370.7	426.4	1.87(23)	0.95(1)	0.80(18)	$5^+ \rightarrow 3^+$
980.6(2)	1370.7	390.1	99.49(1206)	0.51(1)	0.46(6)	$5^+ \rightarrow 4^+$
990.1(2)	5618.7	4629.0	4.02(63)		0.55(28)	$11^- \rightarrow (9^-)$
1001.9(2)	1677.5	674.9	2.41(45)			$5^+ \rightarrow 3^+$
1005.8(2)	1249.5	243.5	0.21(3)	1.75(6)		$4^+ \rightarrow 2^+$
1008.1(2)	6009.1	5000.6	2.43(38)			$11^+ \rightarrow 10^-$
1014.2(3)[a]	4447.6	3435.0	4.11(65)			$9^- \rightarrow 8^-$
1059.3(2)[a]	1485.7	426.4	0.48(8)			$4^+ \rightarrow 3^+$
1068.7(1)	5048.4	3979.5	1.85(29)			$10^- \rightarrow 9^-$
1092.5(2)[a]	7101.6	6009.1	3.26(51)	0.30(1)	−0.33(21)	$12^+ \rightarrow 11^+$
1111.7(4)	7287.4	6175.8	2.36(37)	1.28(4)		$12^+ \rightarrow 10^+$
1118.8(2)	4747.2	3628.4	17.67(277)	0.54(1)	0.23(8)	$9^+ \rightarrow 8^-$
1135.2(2)	4165.7	3029.9	3.96(62)	1.46(4)		$9^- \rightarrow 7^-$
1139.2(2)	3435.0	2295.8	20.04(314)	1.07(2)		$8^- \rightarrow 6^-$
1147.8(4)[a]	2518.5	1370.7	4.23(66)			$6^- \rightarrow 5^+$
1169.0(1)[a]	6217.4	5048.4	3.43(54)			$(11^-) \rightarrow 10^-$
1193.9(1)	4629.0	3435.0	3.82(60)	1.59(3)		$(9^-) \rightarrow 8^-$
1222.3(1)[a]	1921.6	699.3	0.17(3)	1.58(8)		$(5^+) \rightarrow 3^+$
1251.2(2)	1677.5	426.4	1.23(19)	1.56(4)	0.44(40)	$5^+ \rightarrow 3^+$
1253.4(1)	3401.4	2148.0	1.14(18)			$(8^+) \rightarrow 6^+$
1261.9(2)	6009.1	4747.2	7.65(120)	2.08(2)	1.28(22)	$11^+ \rightarrow 9^+$
1273.0(2)	4165.7	2892.7	10.68(167)	1.45(1)	1.12(22)	$9^- \rightarrow 7^-$
1278.3(2)	7287.4	6009.1	2.06(32)	0.61(1)		$12^+ \rightarrow 11^+$
1287.3(1)	1677.5	390.1	2.10(33)			$5^+ \rightarrow 4^+$
1292.4(1)	7132.5	5841.6	0.68(11)			$(13^-) \rightarrow (12^-)$
1332.6(2)	3628.4	2295.8	25.69(402)	1.22(1)	1.05(14)	$8^- \rightarrow 6^-$
1372.7(2)	5000.6	3628.4	3.29(52)	1.24(2)	1.38(39)	$10^- \rightarrow 8^-$
1417.8(2)[a]	4447.6	3029.9	1.06(17)			$9^- \rightarrow 7^-$
1428.6(2)	6175.8	4747.2	2.81(44)	0.96(3)	−0.97(53)	$10^+ \rightarrow 9^+$
1437.6(2)[a]	4629.0	3191.4	3.12(49)	1.90(6)		$(9^-) \rightarrow 6^-$
1462.9(1)	2833.6	1370.7	3.52(55)	1.44(3)		$(7^+) \rightarrow 5^+$
1491.1(2)[a]	1917.5	426.4	1.00(16)	1.67(3)		$5^+ \rightarrow 3^+$
1513.8(1)	7132.5	5618.7	0.85(25)			$(13^-) \rightarrow 11^-$
1514.0(2)[a]	3191.4	1677.5	0.71(24)			$6^- \rightarrow 5^+$
1554.9(2)[a]	4447.6	2892.7	2.99(47)	1.15(2)		$9^- \rightarrow 7^-$
1611.4(3)[a]	7620.5	6009.1	5.08(79)	0.41(1)		$(12^+) \rightarrow 11^+$
1757.5(2)	2148.0	390.1	4.22(26)	1.30(2)	1.21(29)	$6^+ \rightarrow 4^+$
1820.7(2)[a]	3191.4	1370.7	6.56(103)			$6^- \rightarrow 5^+$
1843.3(2)	6009.1	4165.7	0.81(13)			$11^+ \rightarrow 9^-$
1859.2(6)[a]	8960.8	7101.6				$(14^+) \rightarrow 12^+$
1869.7(5)[a]	4165.7	2295.8	1.75(28)			$9^- \rightarrow 6^-$
1906.0(2)	2295.8	390.1	0.79(12)			$6^- \rightarrow 4^+$

[a]Not placed in the partial level scheme shown in Fig. 1.

γ-ray transitions at 567.8 and 1253.4 keV, and one new level (8^+) at 3401.4 keV have been added to structure 2 in the present work.

Typical γ-ray spectra which support the proposed level scheme are shown in Fig. 2, and the measured linear polarizations for some observed transitions in ^{62}Cu are plotted in Fig. 3. With five neutrons and one proton outside the ^{56}Ni doubly magic core, odd-odd ^{62}Cu is located in the lower part of the $p_{3/2}$, $f_{5/2}$, and $p_{1/2}$ subshells for both unpaired protons and neutrons. According to the finite-range droplet model (FRDM) calculations, the ground state of ^{62}Cu was suggested to have a moderate quadrupole deformation ($\beta_2 = 0.15$) [14]. A number of linking transitions between the two low-lying positive-parity structures 1 and 2 have been observed. These two positive-parity structures most likely have similar pf configurations, which will be discussed in the following. It should be noted that besides these two positive-parity structures, many single-particle-type positive-parity levels (not shown

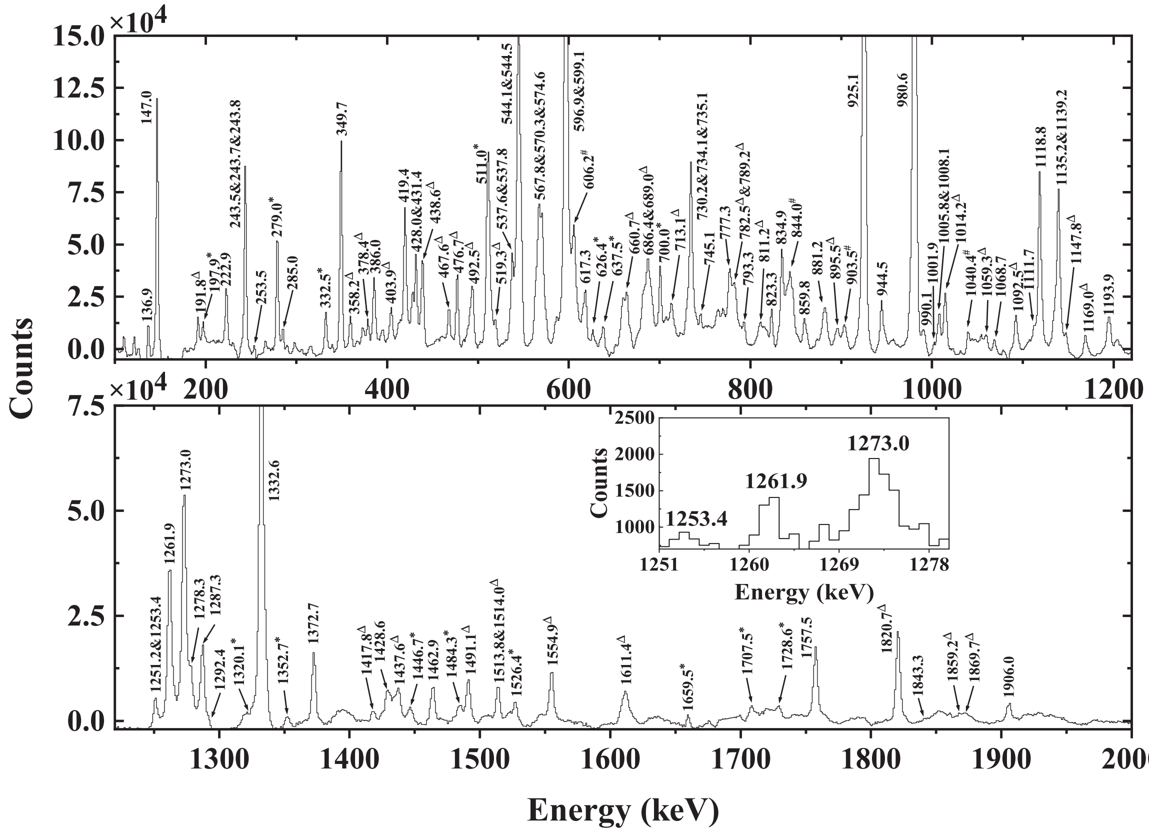

FIG. 2. Coincident γ-ray spectra generated from the sum of gates on 243.5-, 349.7-, and 386.0-keV transitions. The inset in the lower panel: Coincident γ-ray spectrum generated from the sum of gates on 777.3- and 1757.5-keV transitions. The peaks marked with triangles ($\triangle$) belong to ^{62}Cu but are not included in the partial level scheme of Fig. 1, the peaks marked with stars ($*$) are known contaminants from other nuclei, and the peaks marked with hashtags (#) probably belong to ^{62}Cu but are not placed in this paper.

in Fig. 1) have also been observed at low excitation energy. They decay toward these two collective structures and reflect the coexistence of single-particle and collective excitations in ^{62}Cu.

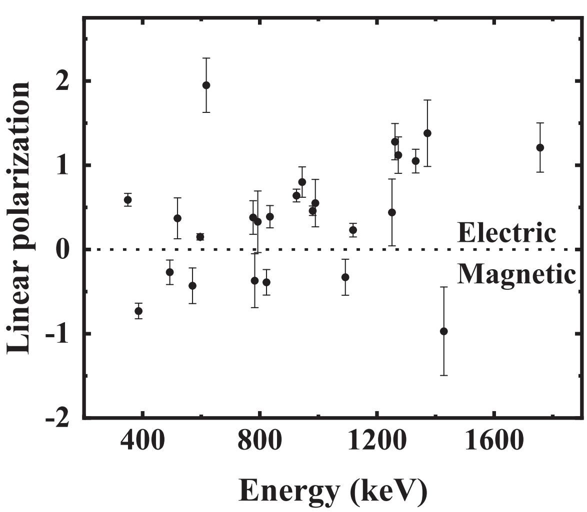

FIG. 3. The linear polarizations for some observed transitions in ^{62}Cu. In general, a positive value corresponds to an electric transition, and a negative value indicates a magnetic transition.

At medium to high excitation energies, three negative-parity structures 3–5 are established. The parity changes relative to the low-lying structures, implying that the configurations of these three negative-parity structures involve an odd number of particles in the $g_{9/2}$ orbital, which will result in a larger deformation. In Ref. [15], the 6^- head of structure 3 was suggested to have a $\pi(pf)^1 \otimes \nu(g_{9/2})^1$ configuration. In the neighboring odd-odd nuclides ^{60}Cu [16] and ^{64}Cu [17], 6^- states have also been observed at similar medium excitation energies and have been suggested to have the same configuration as that of ^{62}Cu. In Fig. 4 , the negative-parity structures built on the 6^- levels in ^{60}Cu [18], ^{62}Cu, and ^{64}Cu [17] are compared. The similarity visible in Fig. 4 further supports the same configuration assignments.

At high excitation energies, a short level structure 6 is also observed. The positive parity implies that its structure involves excitations of additional low-orbit pf nucleons into the $g_{9/2}$ orbital. It has been suggested that the nuclear quadrupole deformation increases with the number of $g_{9/2}$ particles excited [4,19]. Therefore, such a structure may signify a well or highly deformed configuration.

To obtain further insight into the collective structures in ^{62}Cu, TAC-CDFT [9,20,21] calculations are performed. The TAC-CDFT consists of the meson exchange [22] and the point-coupling versions [20], which provides a consistent description of nuclear currents and time-odd fields, and the

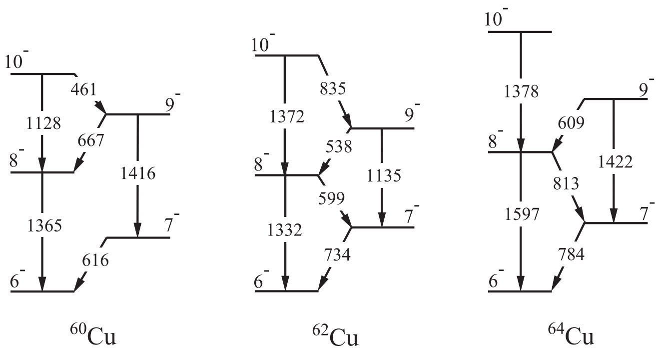

FIG. 4. Comparison of the negative-parity structures built on the 6^- level in ^{60}Cu [18], ^{62}Cu, and ^{64}Cu [17].

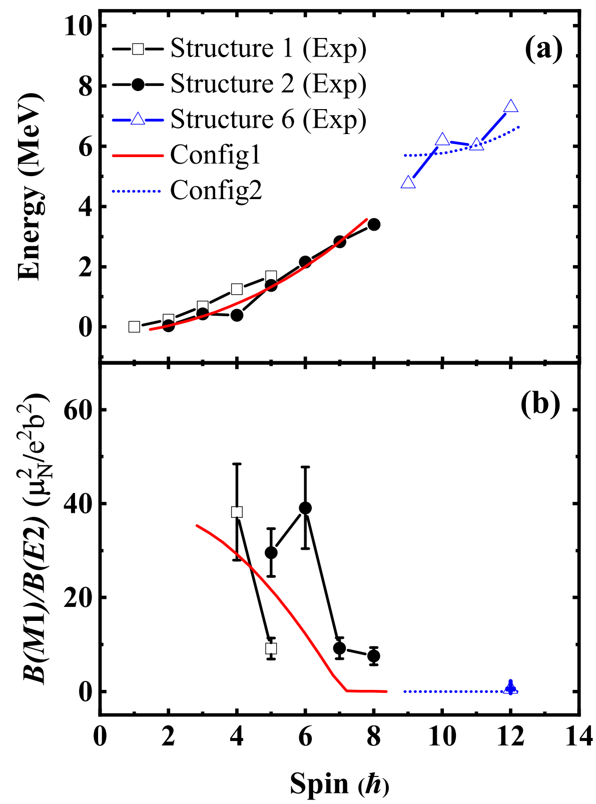

FIG. 5. The calculated (a) energy spectra and (b) $B(M1)/B(E2)$ ratios as a function of spin by TAC-CDFT calculations in comparison with the experimental data for positive-parity structures.

included nuclear magnetism plays important roles for the description of nuclear rotations [23]. The TAC-CDFT has been successfully used to describe the magnetic rotational bands [24,25], antimagnetic rotational bands [21,26], linear-α cluster structure [27,28], etc. Here, the relativistic point-coupling density functional PC-PK1 [29] is adopted in the particle-hole channel. The single-particle Dirac equation is solved in a three-dimensional harmonic-oscillator basis in Cartesian coordinates with ten major shells, which provides convergent results for nuclei in the $A \approx 60$ mass region [20]. In the present calculations, the ground state of ^{62}Cu is found as the $\pi(p_{3/2}f_{5/2})^1 \otimes \nu(p_{3/2}f_{5/2})^5$ configuration with a quadrupole deformation of $\beta_2 = 0.21$ and $\gamma = 39^\circ$, a little larger than the FRDM prediction [14]. It is also found that for ^{62}Cu an excitation into the positive-parity $g_{9/2}$ shell is much easier for the neutron than for the proton. To break the ^{56}Ni core the proton excitation with an $f_{7/2}$ hole is favored over that of the neutron. Therefore, to probe collective structures in ^{62}Cu, we have performed different TAC-CDFT calculations by the configuration-fixed constrained approach [30] for the ground-state configuration (Config1) as well as several excited modes, which include another positive-parity configuration (Config2) with both pf proton and neutron excited into the $g_{9/2}$ orbitals, i.e., $\pi(g_{9/2})^1 \otimes \nu(g_{9/2})^1(p_{3/2}f_{5/2})^4$, and three negative-parity configurations: (Config3) a pf neutron excited into the $g_{9/2}$ orbital, i.e., $\pi(p_{3/2}f_{5/2})^1 \otimes \nu(g_{9/2})^1(p_{3/2}f_{5/2})^4$; (Config4) combining the neutron $g_{9/2}$ particle with the ^{56}Ni proton core breaking, i.e., $\pi(f_{7/2})^{-1}(p_{3/2}f_{5/2})^2 \otimes \nu(g_{9/2})^1(p_{3/2}f_{5/2})^4$; and (Config5) a more excited one that combines the neutron $g_{9/2}$ particle and ^{56}Ni core breaking for both protons and neutrons, i.e., $\pi(f_{7/2})^{-1}(p_{3/2}f_{5/2})^2 \otimes \nu(g_{9/2})^1(f_{7/2})^{-1}(p_{3/2}f_{5/2})^5$. Among these configurations, (Config1) and (Config2) correspond to positive parity while the others correspond to negative parity.

In Fig. 5, the calculated energy spectra and $B(M1, I \rightarrow I-1)/B(E2, I \rightarrow I-2)$ ratios as functions of spin for the positive-parity Config1 and Config2 are compared with experimental data for the positive-parity structures 1, 2, and 6. Here, for simplicity, the $I \rightarrow I-1$ transitions are assumed to be $M1$ transitions, i.e., the mixing ratio is zero. Following TAC-CDFT calculations also indicate contribution of $E2$ to the intensity of $I \rightarrow I-1$ transition is much smaller than that of $M1$, consequently, having little influence on the experimental $B(M1)/B(E2)$ ratio. It can be seen that calculations of Config1 give an overall qualitative description of the characteristics of the structures 1 and 2, which further support the similar pf configuration assignments for these structures. The relatively large deviations between the experimental values and the theoretical results for the excitation energy at spin $4\hbar$ and the $B(M1)/B(E2)$ ratios at spin $6\hbar$ of structure 2 are probably due to the strong interplay between the collective and the single-particle degrees of freedom. Indeed, this 4^+ state has been interpreted as a pure $\pi p_{3/2} \otimes \nu f_{5/2}$ configuration in the interacting boson-fermion-fermion model calculation [7]. It is also noted that, as a kind of mean-field calculation and due to the strong mixing between these pf orbitals, the TAC-CDFT only yields the yrast structure on the basis of the configuration $\pi(p_{3/2}f_{5/2})^1 \otimes \nu(p_{3/2}f_{5/2})^5$. One may resort to the beyond-mean-field techniques, such as angular momentum projection, to reproduce the properties of both structures. For the highly excited positive-parity structure 6, the agreement in energy spectra between experimental data and calculations with Config2 is reasonable in both the bandhead spin ($9\hbar$) and the relative excitation energy ($\approx$6 MeV). According to the calculations, the structure with Config2 is predicted as a principal axis rotation with tilting angle equal to zero due to the significant contributions of neutron and proton $g_{9/2}$ orbitals. The strong odd-even staggering of structure 6 might be ascribed to the strong Coriolis interactions of the neutron and proton $g_{9/2}$ particles. As demonstrated in Ref. [9], the

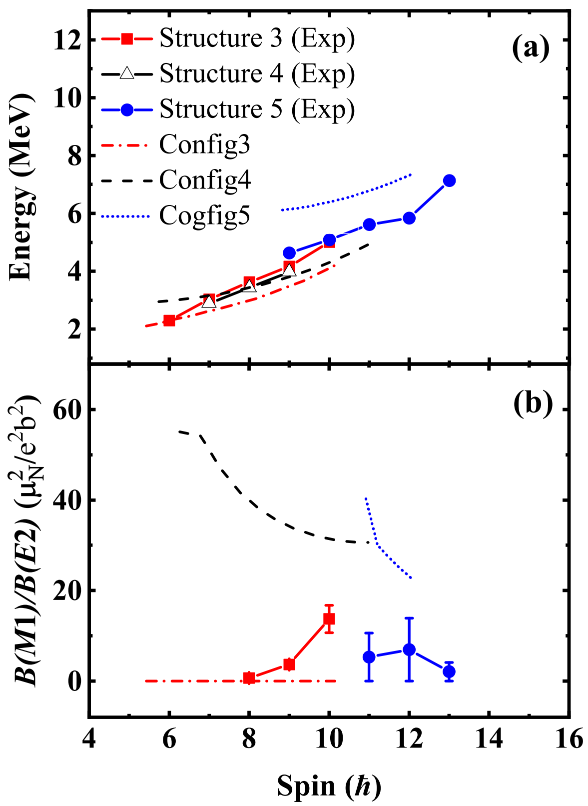

FIG. 6. The calculated (a) energy spectra and (b) $B(M1)/B(E2)$ ratios as a function of spin by TAC-CDFT calculations in comparison with the experimental data for negative-parity structures.

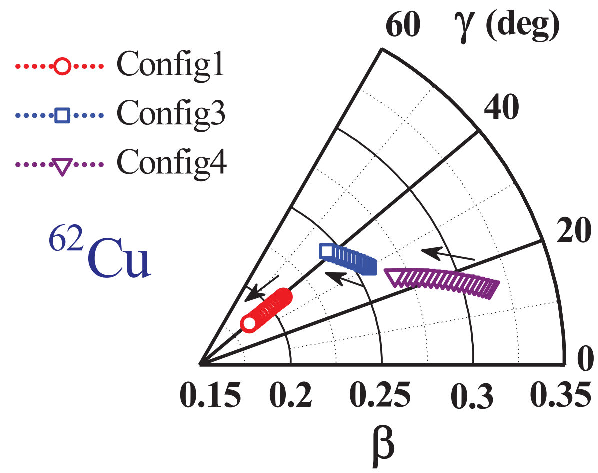

FIG. 7. The evolutions of deformation parameters β and γ driven by increasing rotational frequency in the TAC-CDFT calculations for Config1, Config3, and Config4 in ^{62}Cu.

magnetic moments and, thus, the $B(M1)$ values, vanish in the case of the principal rotation. Therefore, the calculated $B(M1)/B(E2)$ values for Config2 are equal to zero. This is consistent with the observed experimental value at $12\hbar$, which is very close to zero.

Figure 6 shows a comparison of the calculated negative-parity structures with Config3–5 by TAC-CDFT and experimental data for the negative-parity structures 3–5. Similar bandhead spins and excitation energies between experimental and theoretical results suggest that the Config3 or Config4 may be responsible for the structures 3 and 4. The slower increase in the theoretical energies at high spins suggests an overestimation of the moment of inertia for the corresponding configurations. In Fig. 6(b), the calculated $B(M1)/B(E2)$ values for Config3 are equals to zero due to its principle axis rotation (similar to Config2 mentioned above). The small experimental $B(M1)/B(E2)$ values of structure 3 are in accord with the theoretical expectation for Config3. The short structure 4 is tentatively assigned to a magnetic rotation configuration Config4, although the observation of structure 3 lying higher than structure 4 is not reproduced by the TAC-CDFT calculations. The assignment is supported by the following two facts. On one hand, the observation of $M1$ and the nonobservation of $E2$ transitions in structure 4 are in agreement with the large $B(M1)/B(E2)$ values predicted for Config4. On the other hand, the fact that structure 6 decays out to structure 3 but not to structure 4 indicates a discrepancy in intrinsic configuration between structures 3 and 4. For structure 5, the bandhead spin and the increasing trend of energy levels are well reproduced, but there are deviations between experimental data and calculations with Config5 for both bandhead energy and $B(M1)/B(E2)$ values. To firmly determine configuration assignments for structures 4 and 5, more experimental and theoretical studies are desirable.

The calculated evolution of deformation parameters β and γ with rotational frequency for Config1, Config3, and Config4 are shown in Fig. 7. With configurations involving the deformation-driving $1g_{9/2}$ orbital, the β values for Config3 and Config4, typically lie around 0.24–0.26 and 0.26–0.32, respectively, larger than that of Config1, typically lying around 0.19–0.21. The β deformations for Config1, Config3, and Config4 behave in a similar way, i.e., a smooth decrease in β. Meanwhile, the γ value ($\gamma \approx 40^\circ$) of Config1 changes very slightly, and both γ values of Config3 and Config4 show a smoothly increasing tendency.

In the present work, a clear magnetic rotational structure in ^{62}Cu is not found. Only a short dipole structure 4 at the medium excitation energy range is observed. In the mass $A \approx 60$ region, a proton hole in the $f_{7/2}$ shell and a neutron in the $g_{9/2}$ shell are favorable conditions for a nucleus to give rise to magnetic rotation [2], which corresponds to Config4 in this paper. Here, the electromagnetic properties and shears mechanism for Config4 predicted by the TAC-CDFT calculations are discussed in more detail.

Figure 8 shows the calculated reduced transition probabilities, $B(M1)$ and $B(E2)$ for this configuration. It can be seen that its $B(E2)$ values are relatively small and the $B(M1)$ values are big. As the spin increases, the $B(M1)$ values decrease smoothly. Meanwhile, the $B(E2)$ values first decrease a little bit, then increase, and finally decrease. In the TAC-CDFT calculations, the $B(E2)$ values are determined by both the tilting angle and the quadrupole moment. As shown in Fig. 9, the tilting angle of the total angular momentum decreases with rotational frequencies, which would lead to an increase in the $B(E2)$ values. Meanwhile, the quadrupole moment of the

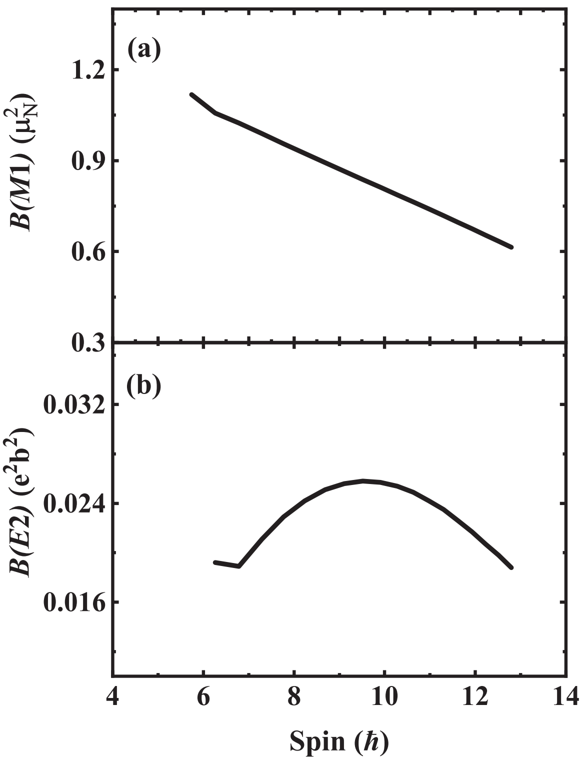

FIG. 8. The calculated reduced transition probabilities (a) $B(M1)$ and (b) $B(E2)$ for Config4.

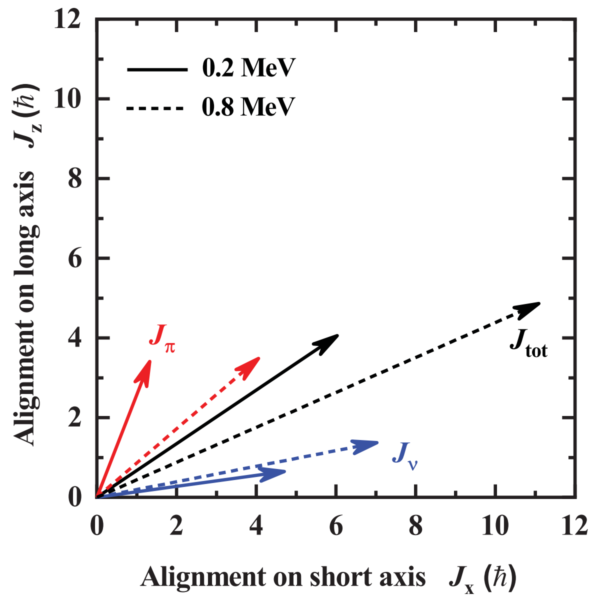

FIG. 9. Composition of proton and neutron angular momentum vectors J_π and J_ν, as well as the total angular momentum vector $J_{tot} = J_\pi + J_\nu$ at both the low rotational frequency ≈ 0.2 MeV and the high rotational frequency ≈ 0.8 MeV in the TAC-CDFT calculations with Config4.

predicted magnetic rotational band is found to decrease with spin (shown in Fig. 7), and this, in turn, would decrease the $B(E2)$ values. In the lower spin region, the decrease in the tilting angle dominates the evolution of $B(E2)$ values and, therefore, an enhancement of $B(E2)$ values is obtained. In the higher spin region, however, the decrease in quadrupole moment dominates, and this leads to the decrease in the $B(E2)$ values. Therefore, the competition between the tilting angle and the quadrupole moment results in the observed behavior of $B(E2)$ values with spin shown in Fig. 8.

To examine the angular momentum forming mechanism of this configuration, the proton and neutron angular momentum vectors J_π and J_ν as well as the total angular momentum vector $J_{tot} = J_\pi + J_\nu$, at both the low rotational frequency ≈ 0.2 MeV and high rotational frequency ≈ 0.8 MeV in the TAC-CDFT calculations for Config4 are shown in Fig. 9. Here the proton and neutron angular momenta J_π and J_ν are the summation of the expectation values of the angular momenta over all the proton and neutron orbitals occupied in the cranking wave function in the intrinsic system, respectively. In the TAC-CDFT calculations, both angular momentum components along the short and the long principal axes of nuclear density distribution can be obtained.

As shown in Fig. 9, the protons mainly contribute to the angular momentum along the z axis, but little along the x axis, whereas the neutrons contribute a large J_x component but a small J_z component. With the increase of rotational frequency, both J_π and J_ν move toward the direction of the total angular momentum. Consequently, the tilting angle of the total angular momentum does not change much, suggesting a good shears mechanism for this configuration. Identifying such magnetic rotational structure in ^{62}Cu in future experiments is meaningful.

IV. SUMMARY

The spectroscopy of ^{62}Cu was studied via the ^{54}Cr(^{12}C, $1p3n$) ^{62}Cu fusion-evaporation reaction at a beam energy of 67 MeV. Three positive-parity level sequences (structures 1, 2, and 6) and three negative-parity level sequences (structures 3–5) are observed. The properties of these collective structures in ^{62}Cu are investigated in terms of the TAC-CDFT with different configurations.

For the positive-parity structures 1, 2, and 6, the agreements between the experimental data and the calculations are reasonable. The calculated energy spectra and $B(M1)/B(E2)$ ratios by TAC-CDFT with $\pi(p_{3/2}f_{5/2})^1 \otimes \nu(p_{3/2}f_{5/2})^5$ configuration give an overall qualitative description of the characteristic features of structures 1 and 2, which is consistent with the systematics of these nuclear configurations in this region. Meanwhile, structure 6 is most likely to have a $\pi(g_{9/2})^1 \otimes \nu(g_{9/2})^1(p_{3/2}f_{5/2})^4$ configuration.

For the negative-parity structures 3–5, similar bandhead spin and excitation energy between experimental and theoretical results suggest that the $\pi(p_{3/2}f_{5/2})^1 \otimes \nu(g_{9/2})^1(p_{3/2}f_{5/2})^4$ and $\pi(f_{7/2})^{-1}(p_{3/2}f_{5/2})^2 \otimes \nu(g_{9/2})^1(p_{3/2}f_{5/2})^4$ configurations may be associated with structures 3 and 4, although the calculations slightly overestimate the moment of inertia for these configurations. The configuration for structure 5 is not determined due to the deviations between the experimental data and the calculations. The evolutions of the deformation parameters β and γ driven as a function of the rotational frequency in the TAC-CDFT calculations are presented.

The properties of the possible magnetic rotational structure with $\pi(f_{7/2})^{-1}(p_{3/2}f_{5/2})^2 \otimes \nu(g_{9/2})^1(p_{3/2}f_{5/2})^4$ configuration have been discussed. Examination of its angular momentum forming mechanism shows dominating shears mechanism. Identifying this interesting shears configuration in ^{62}Cu calls for more experimental studies.

ACKNOWLEDGMENTS

This work was supported by the National Key R&D Program of China (Contract No. 2018YFA0404403), the National Natural Science Foundation of China under Grants No. 12035001, No. 12075006, No. 11875075, and No. 11675003, and the National Research Foundation of South Africa under Grant No. 09741. We wish to thank Dr. Q. W. Fan for making the target and the staff of iThemba LABS for their support.

[1] D. Steppenbeck, R. V. F. Janssens, S. J. Freeman, M. P. Carpenter, P. Chowdhury, A. N. Deacon, M. Honma, H. Jin, T. Lauritsen, C. J. Lister, J. Meng, J. Peng, D. Seweryniak, J. F. Smith, Y. Sun, S. L. Tabor, B. J. Varley, Y.-C. Yang, S. Q. Zhang, P. W. Zhao *et al.*, Phys. Rev. C **85**, 044316 (2012).

[2] D. A. Torres, F. Cristancho, L.-L. Andersson, E. K. Johansson, D. Rudolph, C. Fahlander, J. Ekman, R. du Rietz, C. Andreoiu, M. P. Carpenter, D. Seweryniak, S. Zhu, R. J. Charity, C. J. Chiara, C. Hoel, O. L. Pechenaya, W. Reviol, D. G. Sarantites, L. G. Sobotka, C. Baktash *et al.*, Phys. Rev. C **78**, 054318 (2008).

[3] D. Rudolph, C. Baktash, J. Dobaczewski, W. Nazarewicz, W. Satuła, M. J. Brinkman, M. Devlin, H.-Q. Jin, D. R. LaFosse, L. L. Riedinger, D. G. Sarantites, and C.-H. Yu, Phys. Rev. Lett. **80**, 3018 (1998).

[4] C. Andreoiu, D. Rudolph, C. E. Svensson, A. V. Afanasjev, J. Dobaczewski, I. Ragnarsson, C. Baktash, J. Eberth, C. Fahlander, D. S. Haslip, D. R. LaFosse, S. D. Paul, D. G. Sarantites, H. G. Thomas, J. C. Waddington, W. Weintraub, J. N. Wilson, and C.-H. Yu, Phys. Rev. C **62**, 051301(R) (2000).

[5] L. L. Andersson, D. Rudolph, E. K. Johansson, D. A. Torres, B. G. Carlsson, I. Ragnarsson, C. Andreoiu, C. Baktash, M. P. Carpenter, R. J. Charity, C. J. Chiara, J. Ekman, C. Fahlander, C. Hoel, O. L. Pechenaya, W. Reviol, R. du Rietz, D. G. Sarantites, D. Seweryniak, L. G. Sobotka *et al.*, Eur. Phys. J. A **36**, 251 (2008).

[6] A. L. Nichols, B. Singh, and J. K. Tuli, Nucl. Data Sheets **113**, 973 (2012).

[7] A. K. Singh, G. Gangopadhyay, D. Banerjee, R. Bhattacharya, R. K. Bhowmik, S. Muralithar, R. P. Singh, A. Mukherjee, U. D. Pramanik, A. Goswami, S. Chattopadhyay, S. Bhattacharya, B. Dasmahapatra, and S. Sen, Phys. Rev. C **59**, 2440 (1999).

[8] B. Mukherjee, S. Muralithar, R. P. Singh, R. Kumar, K. Rani, and R. K. Bhowmik, Phys. Rev. C **63**, 057302 (2001).

[9] J. Meng, J. Peng, S.-Q. Zhang, and P.-W. Zhao, Front. Phys. **8**, 55 (2013).

[10] J. Sharpey-Schafer, Nucl. Phys. News **14**, 5 (2004).

[11] D. Radford, Nucl. Instrum. Methods Phys. Res., Sect. A **361**, 297 (1995).

[12] M. Piiparinen, A. Ataç, J. Blomqvist, G. Hagemann, B. Herskind, R. Julin, S. Juutinen, A. Lampinen, J. Nyberg, G. Sletten, P. Tikkanen, S. Törmänen, A. Virtanen, and R. Wyss, Nucl. Phys. **A605**, 191 (1996).

[13] P. Jones, L. Wei, F. Beck, P. Butler, T. Byrski, G. Duchêne, G. de France, F. Hannachi, G. Jones, and B. Kharraja, Nucl. Instrum. Methods Phys. Res., Sect. A **362**, 556 (1995).

[14] P. Möller, A. J. Sierk, T. Ichikawa, and H. Sagawa, At. Data Nucl. Data Tables **109–110**, 1 (2016).

[15] T. U. Chan, M. Agard, J. F. Bruandet, A. Giorni, F. Classer, J. P. Longequeue, and C. Morand, Nucl. Phys. A **293**, 207 (1977).

[16] U. Fister, R. Jahn, P. von Neumann-Cosel, P. Schenk, T. Trelle, D. Wenzel, and U. Wienands, Nucl. Phys. A **569**, 421 (1994).

[17] S. Samanta, S. Das, R. Bhattacharjee, S. Chatterjee, R. Raut, S. S. Ghugre, A. K. Sinha, U. Garg, Neelam, N. Kumar, P. Jones, M. S. R. Laskar, F. S. Babra, S. Biswas, S. Saha, P. Singh, and R. Palit, Phys. Rev. C **97**, 014319 (2018).

[18] O. Izotova, D. Rudolph, J. Ekman, C. Fahlander, A. Algora, C. Andreoiu, R. Cardona, C. Chandler, G. de Angelis, E. Farnea, A. Gadea, J. Garcés Narro, J. Nyberg, M. Palacz, Z. Podolyák, T. Steinhardt, and O. Thelen, Phys. Rev. C **69**, 037303 (2004).

[19] C. Andreoiu, D. Rudolph, I. Ragnarsson, C. Fahlander, R. A. E. Austin, M. P. Carpenter, R. M. Clark, J. Ekman, R. V. F. Janssens, T. L. Khoo, F. G. Kondev, T. Lauritsen, T. Rodinger, D. G. Sarantites, D. Seweryniak, T. Steinhardt, C. E. Svensson, O. Thelen, and J. C. Waddington, Eur. Phys. J. A **14**, 317 (2002).

[20] P. W. Zhao, S. Q. Zhang, J. Peng, H. Z. Liang, P. Ring, and J. Meng, Phys. Lett. B **699**, 181 (2011).

[21] P. W. Zhao, J. Peng, H. Z. Liang, P. Ring, and J. Meng, Phys. Rev. Lett. **107**, 122501 (2011).

[22] J. Peng, J. Meng, P. Ring, and S. Q. Zhang, Phys. Rev. C **78**, 024313 (2008).

[23] J. Meng, *Relativistic Density Functional for Nuclear Structure*, International Review of Nuclear Physics, Vol. 10 (World Scientific, Singapore, 2016).

[24] L. F. Yu, P. W. Zhao, S. Q. Zhang, P. Ring, and J. Meng, Phys. Rev. C **85**, 024318 (2012).

[25] Y. K. Wang, Phys. Rev. C **97**, 064321 (2018).

[26] P. W. Zhao, J. Peng, H. Z. Liang, P. Ring, and J. Meng, Phys. Rev. C **85**, 054310 (2012).

[27] P. W. Zhao, N. Itagaki, and J. Meng, Phys. Rev. Lett. **115**, 022501 (2015).

[28] Z. X. Ren, S. Q. Zhang, P. W. Zhao, N. Itagaki, J. A. Maruhn, and J. Meng, Sci. China: Phys., Mech. Astron. **62**, 112062 (2019).

[29] P. W. Zhao, Z. P. Li, J. M. Yao, and J. Meng, Phys. Rev. C **82**, 054319 (2010).

[30] J. Meng, J. Peng, S. Q. Zhang, and S.-G. Zhou, Phys. Rev. C **73**, 037303 (2006).